RESEARCH ARTICLE

small methods
www.small-methods.com

Rational Design of Perforated Bimetallic (Ni, Mo) Sulfides/N-doped Graphitic Carbon Composite Microspheres as Anode Materials for Superior Na-Ion Batteries

Jae Seob Lee, Rakesh Saroha, Se Hwan Oh, Dong Hyeok Shin, Sang Mun Jeong, Jae-Kwang Kim, and Jung Sang Cho**

Highly conductive 3D ordered mesoporous Ni_7S_6-MoS_2/N-doped graphitic carbon (NGC) composite (P-NiMoS/C) microspheres are prepared as anode materials for Na-ion batteries. The rationally designed nanostructure comprises stable Ni_7S_6- and MoS_2-phases along with the homogeneously distributed ordered mesopores ($\phi = 50$ nm) over the external and internal structures generated through thermal decomposition of polystyrene nanobeads ($\phi = 100$ nm). Therefore, the P-NiMoS/C microspheres deliver initial discharge capacities of 662, 419, 373, 300, 231, 181, and 146 mA h g^{-1} at current densities of 0.5, 1, 2, 4, 6, 8, and 10 A g^{-1}, respectively. Furthermore, P-NiMoS/C exhibits a stable discharge capacity of 444 mA h g^{-1} at the end of the 150th cycle at a current density of 0.5 A g^{-1}, indicating higher cycling stability than the filled, that is, non-mesoporous, Ni_3S_2-MoS_2/NGC (F-NiMoS/C) microspheres and filled carbon-free Ni_3S_2-MoS_2 (F-NiMoS) microspheres. The superior electrochemical performance of P-NiMoS/C microspheres is attributed to the rapid Na^+ ion diffusion, alleviation of severe volume stress during prolonged cycling, and higher electrical conductivity of NGC, which results in fast charge transfer during the redox processes. The results in the present study can provide fundamental knowledge for the development of multicomponent, porous, and highly conductive anodes for various applications.

1. Introduction

Layered transition metal sulfides, such as MoS_2, WS_2, FeS_2, and SnS_2, have drawn considerable attention worldwide owing to their unique layered structure with large interlayer spacing, high specific capacity through intercalation, alloying and conversion reactions, and low processing cost, which makes them promising anode materials for Li- and Na-ion batteries (LIBs and NIBs).[1–8] However, their widespread use has been inhibited by the low electronic conductivity and large volume variation of the structure during repeated charging and discharging, which result in the pulverization of the electrodes and hence, rapid capacity decay.[6,9,10] To overcome these drawbacks, numerous rationally designed 2D layered electrode materials with different morphologies, such as aerogels,[8] nanosheets,[11] nanoplatelets,[12] nanoflowers,[7,13] nanofibers,[14–16] yolk–shell,[17,18] and even composites,[2,19] have been synthesized and studied as anodes.

Bimetallic sulfides (BMSs) have also been rigorously studied owing to their high electronic conductivity and efficient electrochemical activity.[20] The use of two metals rather than one provides synergetic advantages in terms of mechanical stability and electrochemical controllability over metallic oxides and monometallic sulfides.[21] It has been reported that suitable transition metal doping effectively reduces the particle size of the electrode material, which subsequently leads to lower cell resistance and enhanced performance.[22] Along with higher mechanical stability, BMSs also offer better electronic/ionic conductivity owing to the presence of multiple metal species. Moreover, several studies focused on the further enhancement of the electrical conductivity of these BMSs by combining them with carbonaceous materials, such as reduced-graphene oxides (rGOs) and carbon nanotubes (CNTs).[21,23] For example, Xu et al. reported BMS nanoparticles synthesized by the pyrolysis of surface-intercalated layered double hydroxide and melamine, which are well protected by rGO and N-doped CNTs.[24] Similarly, Zhu et al. applied a bottom–up approach to prepare bimetallic (Ni, Co) sulfide nanocrystals well-embedded into N-doped carbon core–shell nanocubes.[25]

The porosity of the electrode materials is another crucial parameter for the electrochemical performance of materials. The porous channels or network in the structure of electrode

---

J. S. Lee, R. Saroha, S. H. Oh, D. H. Shin, J. S. Cho
Department of Engineering Chemistry
Chungbuk National University
Chungbuk 361-763, Republic of Korea
E-mail: jscho@cbnu.ac.kr

S. M. Jeong
Department of Chemical Engineering
Chungbuk National University
Chungbuk 361-763, Republic of Korea

J.-K. Kim
Department of Solar & Energy Engineering
Cheongju University
Cheongju, Chungbuk 28503, Republic of Korea
E-mail: jaekwang@cju.ac.kr

The ORCID identification number(s) for the author(s) of this article can be found under https://doi.org/10.1002/smtd.202100195.

DOI: 10.1002/smtd.202100195

materials greatly enhances the electrolyte percolation and decreases ion diffusion lengths during cycling.[9] Furthermore, the porous network structure increases the effective surface area of electrode materials, which in turn acts as a buffer to absorb the undesired volume variations, thereby reducing the pulverization phenomenon.[22] Based on this viewpoint, various porous nanomaterials have been studied and exhibited reasonable cyclic stability and rate capability as anode materials for LIBs and NIBs.[9,13] However, the strategy of combining multicomponent transition metal compounds with a highly conductive carbon framework and numerous uniformly distributed mesopores for NIBs is still in the infancy stage. To the best of our knowledge, 3D ordered mesoporous (3-DOM) BMS-based microspheres encapsulated by N-doped graphitic carbon (NGC) as NIB anodes have not been reported so far.

Based on the above discussion, we carried out a detailed investigation on the facile synthesis of mesoporous Ni_7S_6-MoS_2/NGC composite microspheres comprising a 3-DOM/NGC network (denoted as P-NiMoS/C microspheres) as an anode material for NIBs. The microspheres are synthesized using easily scalable spray pyrolysis followed by a sulfidation process. A polystyrene (PS) nanobeads suspension ($\phi = 100$ nm) was used as a pore-generator for numerous ordered mesopores throughout the structure. In addition, the presence of NGC guarantees high electrical conductivity and fast ionic/electronic transfer, which in turn enhances the redox process. As a result, the obtained rationally designed nanostructure exhibits stable cycling performance and rate capabilities. The Na-ion storage performance of the synthesized P-NiMoS/C microspheres was compared to that of filled (i.e., non-mesoporous) Ni_3S_2-MoS_2/NGC composite (F-NiMoS/C) microspheres and filled carbon-free Ni_3S_2-MoS_2 composite (F-NiMoS) microspheres.

2. Results and Discussion

The detailed procedures for the synthesis of 3-DOM bimetallic (Ni, Mo) sulfide-based N-doped GC composite microspheres along with filled and carbon-free microspheres through easily scalable spray pyrolysis technique are elaborated in **Scheme 1**. The droplets generated by the ultrasonic nebulizer comprised a colloidal solution of homogeneously mixed Ni and Mo-metal precursors, PVP as a carbon source, and PS nanobeads (ϕ = 100 nm) as porogens in distilled water, as shown in Scheme 1-①. The droplets were then passed through the vertical quartz reactor tube maintained at 700 °C (Scheme S1, Supporting Information), resulting in the thermal breakdown of metal precursors to respective metal oxides or metals, whereas PVP decomposed to amorphous carbon. The removal of PS nanobeads as gas products during spray pyrolysis resulted in the formation of uniformly distributed ordered mesopores throughout the microsphere structure. This resulted in the formation of 3-DOM composite microspheres with mixed phases of $NiMoO_4$, MoO_2, and Ni in the carbon matrix. The sulfidation process of the bimetallic oxides/amorphous carbon microspheres obtained after spray pyrolysis was performed

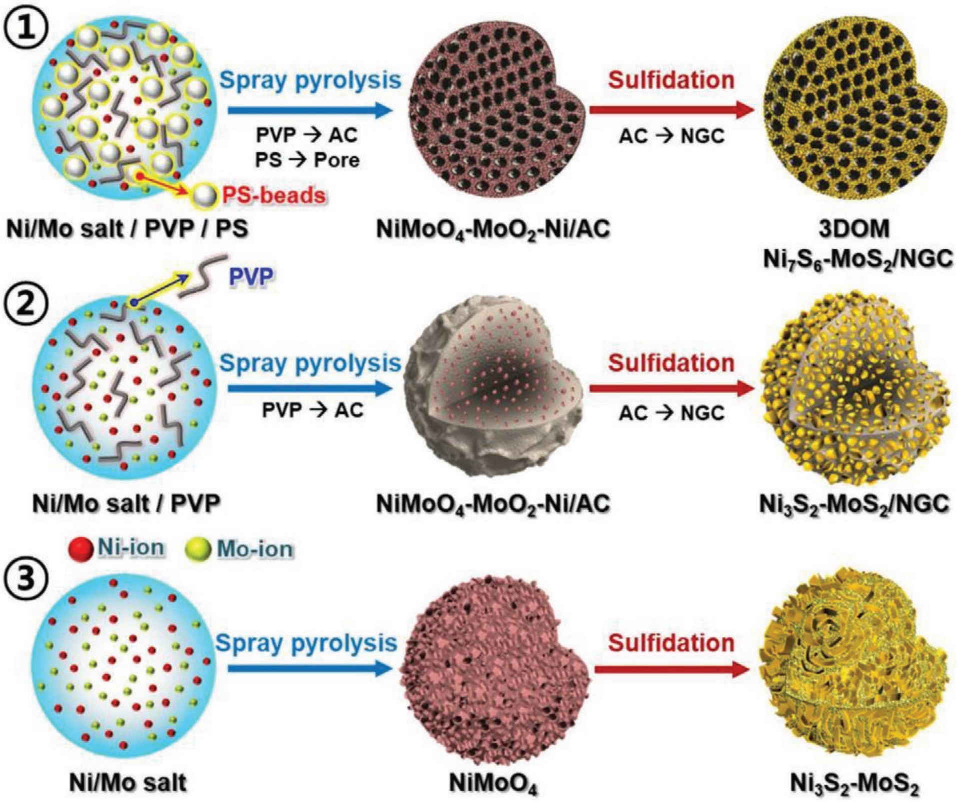

Scheme 1. Schematic representation of formation mechanism of (1-①) 3-DOM Ni_7S_6-MoS_2/NGC, (1-②) filled Ni_3S_2-MoS_2/NGC, and (1-③) carbon-free filled Ni_3S_2-MoS_2 microspheres.

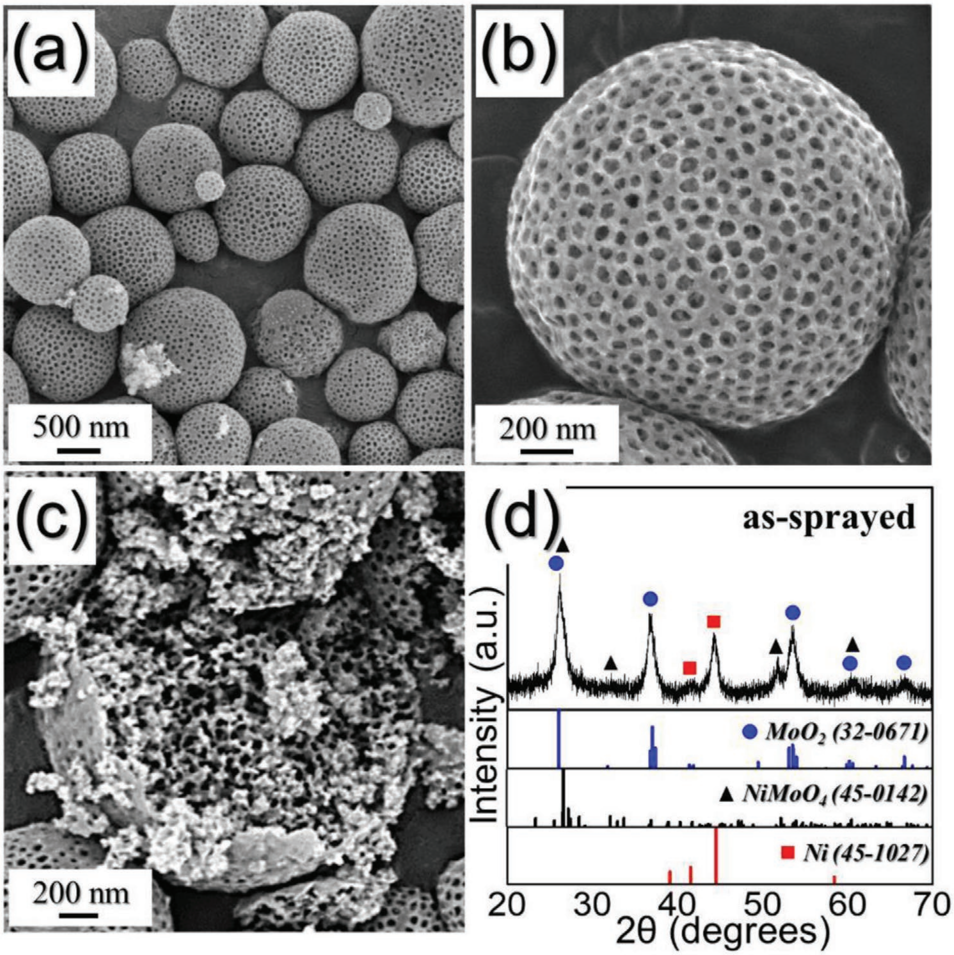

Figure 1. a,b) FE-SEM images, c) fractured sphere's FE-SEM image, and d) XRD pattern of the porous Ni-Mo-C composite microspheres obtained after spray pyrolysis at 700 °C.

using thiourea as a source of sulfur and nitrogen at 500 °C in a reductive atmosphere that subsequently produced 3-DOM Ni_7S_6-MoS_2/NGC composite microspheres (P-NiMoS/C). Additionally, the amorphous carbon decomposed from PVP was further transformed to NGC by the assistance of Ni as a catalyst for graphitization. Likewise, the filled Ni_3S_2-MoS_2/NGC microspheres (F-NiMoS/C; without PS nanobeads in droplets) and filled/carbon-free Ni_3S_2-MoS_2 microspheres (F-NiMoS; without PS nanobeads and PVP in droplets) were also prepared, as shown in Scheme 1-② and 1-③, respectively.

To elucidate the formation mechanism, a comprehensive analysis was performed to confirm the morphological and crystal structure of the obtained microspheres at each step. **Figure 1** shows the microstructural and phase analysis results of the 3-DOM bimetallic (Ni-Mo-C) composite precursors obtained after spray pyrolysis. The field-emission scanning electron microscope (FE-SEM) image (Figure 1a) shows the formation of non-aggregated microspheres with an average diameter of 0.9 µm (Figure S1a, Supporting Information). In addition, the presence of ordered mesopores with average pore diameter of 50 nm (Figure S1b, Supporting Information) over the external surface of the microspheres is also evident from Figure 1b. The formation of such highly ordered mesopores could be attributed to the decomposition of PS nanobeads (ϕ = 100 nm) at 700 °C during spray pyrolysis. Additionally, the heating process results in the contraction of the microspheres, which subsequently leads to shrinkage of the pore diameter from 100 to 40 nm of the powders after spray pyrolysis. The presence of uniformly distributed mesopores in the internal structure was also clearly confirmed by the fractured surface image (Figure 1c). The X-ray diffraction (XRD) pattern of the as-sprayed powders shown in Figure 1d indicates the coexistence of sharp and broad diffraction peaks that are assigned to the mixed phases of MoO_2, $NiMoO_4$, metallic Ni, and amorphous carbon.

The multicomponent 3-DOM composite precursor powders were further subjected to the sulfidation process. Thiourea was used as a sulfur and nitrogen source at 500 °C in a slightly reductive atmosphere. **Figure 2** shows the morphologies and crystal structure of the P-NiMoS/C microspheres obtained after sulfidation. The low-resolution FE-SEM image (Figure 2a) reveals that the obtained P-NiMoS/C microspheres maintained their spherical shape (average diameter of ≈0.9 µm) with a uniform distribution of ordered mesopores throughout the external and internal structures (Figure 2b,c). The

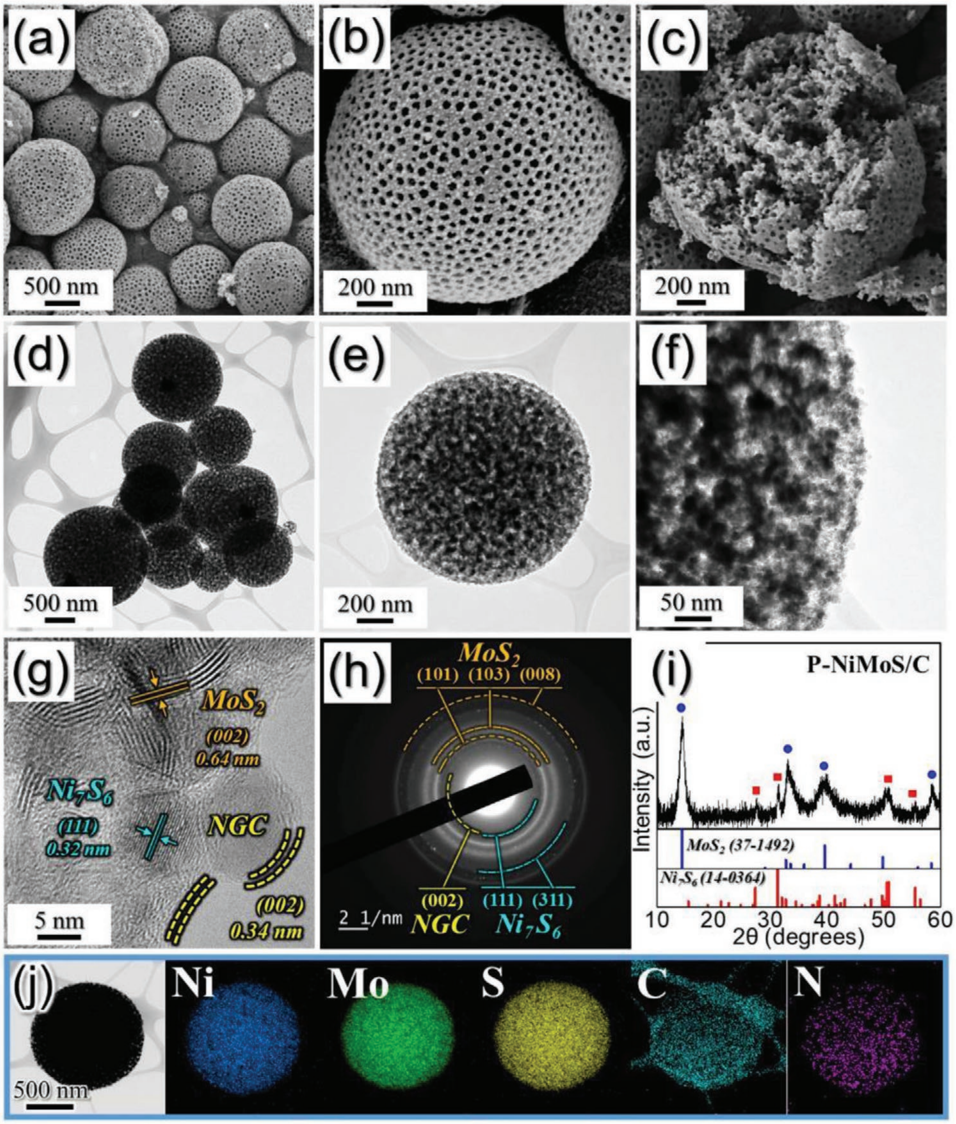

Figure 2. Morphologies, SAED, XRD patterns, and elemental mapping images of P-NiMoS/C microspheres prepared by spray pyrolysis and subsequent sulfidation at 500 °C: a,b) FE-SEM images, c) fractured sphere's FE-SEM image, d–f) TEM images, g) HR-TEM image, h) SAED pattern, i) XRD pattern, and j) elemental mapping images.

transmission electron microscopy (TEM) image (Figure 2d) clearly indicates the formation of spherical, uniformly distributed, and non-aggregated microspheres. Additionally, the TEM images (Figure 2e,f) reveal the uniform distribution of mesopores and multicomponent material as bright and dark spots, respectively. The high-resolution TEM image shown in Figure 2g reveals well-resolved lattice fringes of multicomponent nanocrystal phases. The fringe separations of 0.32 and 0.64 nm correspond to the (111) and (002) lattice planes of the Ni_7S_6 and layered MoS_2 phases, respectively. In addition, a fringe separation of 0.34 nm corresponding to the (002) crystal plane of NGC was also observed, which resulted from the carbonization of PVP and subsequent graphitization of amorphous carbon under a H_2/Ar atmosphere catalyzed by metallic Ni despite the relatively low temperature of 500 °C. The NGC layer surrounding the active materials enhances the overall electrical conductivity of the microspheres owing to the high electronegativity of the nitrogen atom compared to that of the carbon atom.[14,26] The selected area electron diffraction (SAED) pattern (Figure 2h) displays well-resolved diffraction rings that correspond to the MoS_2, Ni_7S_6, and NGC phases. The XRD pattern shown in Figure 2i also shows sharp peaks primarily associated with the biphasic crystal structure of nanocrystalline MoS_2 and Ni_7S_6. The diffraction peaks associated with MoS_2 are more prominent than those associated with Ni_7S_6. The elemental mapping results shown in Figure 2j reveal the homogeneous distribution of Ni, Mo, S, C, and N in the P-NiMoS/C microspheres. Overall, the above results indicate that the presence of two distinct stable phases, the NGC layer, and numerous ordered mesopores in the P-NiMoS/C microspheres enhance the electrochemical performance owing to the enhanced conductivity and better electrolyte percolation.

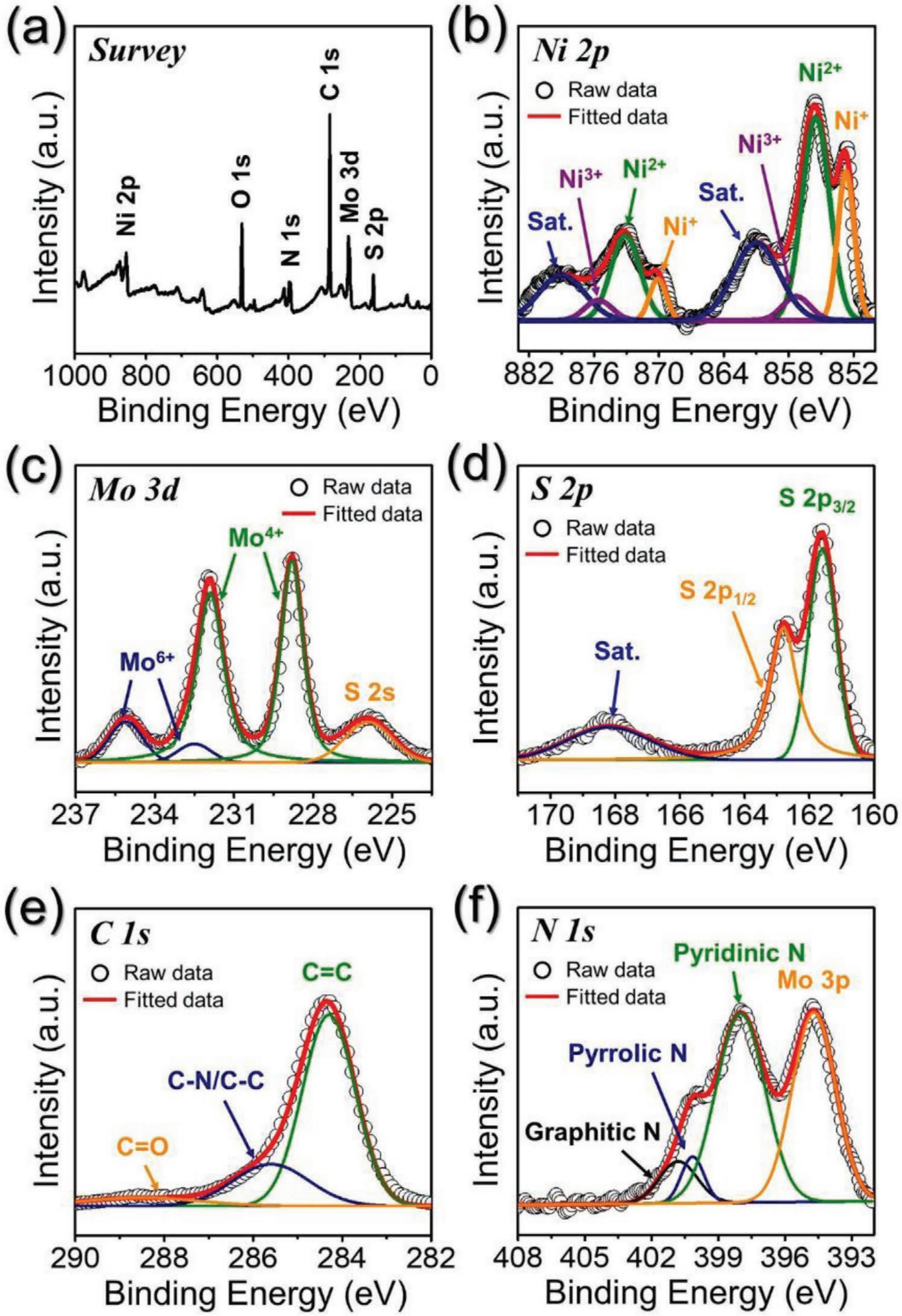

Figure 3. a) XPS survey spectrum and core-level XPS spectra of b) Ni 2p, c) Mo 3d, d) S 2p, e) C 1s, and f) N 1s of P-NiMoS/C microspheres.

The chemical environment of various elements in the P-NiMoS/C microspheres was further determined from X-ray photoelectron spectroscopy (XPS) results. The XPS survey spectrum shown in **Figure 3**a comprises photoelectron signals corresponding to various elements, including Ni 2p, Mo 3d, S 2p, C 1s, N 1s, and O 1s. The Ni 2p spectrum shown in Figure 3b displays well-defined peaks corresponding to the two spin-orbit doublets, that is, Ni $2p_{3/2}$ and Ni $2p_{1/2}$, along with the two shakeup satellite peaks of Ni (denoted as "Sat."). The deconvoluted spectrum reveals that the peak pair centered at 855.5 eV for Ni $2p_{3/2}$ and 873.1 eV for Ni $2p_{1/2}$ could be assigned to the Ni^{2+}.[27,28] Additionally, the peak pair located at 857.3 eV for Ni $2p_{3/2}$ and 875.6 eV for Ni $2p_{1/2}$ correspond to the Ni^{3+} state.[27,28] Moreover, the peaks located at 852.7 and 870.0 eV are attributed to the small traces of Ni_3S_2 in the sample, which agree well with previous reports.[29,30] The deconvoluted Mo 3d spectrum

(Figure 3c) consists of two well-resolved peaks at binding energies of 228.8 and 231.9 eV, which correspond to Mo $3d_{5/2}$ and Mo $3d_{3/2}$, respectively, suggesting the presence of Mo^{4+} species in the form of MoS_2 phase.[9,27,31] In addition, the peak at binding energy of 235.2 eV corresponds to the Mo^{6+} state, indicating the presence of MoO_3 phase, which is believed to be induced by the partial oxidation of the MoS_2 surface owing to the high reactivity of metal sulfide and oxygen.[27,31] Furthermore, a low intensity peak at a binding energy of 225.9 eV from S 2s suggests Mo—S bonding.[31] The deconvoluted S 2p spectrum shown in Figure 3d exhibits two main peaks at binding energies of 162. 8 eV for S $2p_{1/2}$ and 161.6 eV for S $2p_{3/2}$, indicating metal—S bonding.[32] In addition, one shakeup satellite peak at 168.2 eV was observed, which is in good agreement with the previous reports.[33] The C 1s spectrum in Figure 3e is deconvoluted into three distinct peaks at binding energies of 284.3, 285.6, and 288.5 eV, corresponding to the C—C (sp^2), C—C/C—N, and C=O species, respectively.[26,34] The highest intensity of the C=C peak exhibited the formation of graphitic carbon during the sulfidation process. In addition, the presence of the C—N/C—C peak suggests the presence of an NGC framework. The N 1s spectrum shown in Figure 3f displays three well-resolved peaks at binding energies of 398.0, 400.2, and 401.1 eV for pyridinic N, pyrrolic N, and graphitic N, respectively, which is in good agreement with the previous results.[35] Moreover, a sharp peak at 394.7 eV corresponding to the Mo 3p orbital was also observed due to MoS_2 phase.[35,36]

Raman spectroscopy result of the carbon matrix in the P-NiMoS/C microspheres is shown in **Figure 4**a. The well-known signatures of the D- and G-bands at 1348 and 1590 cm^{-1}, respectively, were confirmed. The relative intensity ratio (I_D/I_G) of the D and G bands measures the degree of crystallinity of the carbonaceous material.[14,26,37] The I_D/I_G value of 0.60 of the P-NiMoS/C microspheres indicates that the carbon matrix of the P-NiMoS/C microspheres was mainly graphitic carbon, which is consistent with the TEM result (Figure 2g). Additionally, the Raman spectrum shows well-resolved peaks at 281.1, 378.7, 403.9, and 452.2 cm^{-1}, which correspond to the Mo—S bonds.[38] In addition, slightly broad and low intensity peaks linked to the Ni—S bonds were also observed at 218.1 and 589.6 cm^{-1}.[39,40] The thermogravimetric (TG) curve shown in Figure 4b indicates the amount of NGC matrix in the P-NiMoS/C microspheres. The end-products obtained after the TG analyses were bimetallic oxide ($NiMoO_4$ phase) along with the small traces of NiO phase (Figure S2b, Supporting Information). From this, the content of NGC matrix in P-NiMoS/C microspheres was calculated as 15 wt%. In detail, the amounts of C and N in the composite were 13 and 2 wt%, respectively, from the TG and EA results (Table S1, Supporting Information). The N_2 adsorption–desorption isotherms of the

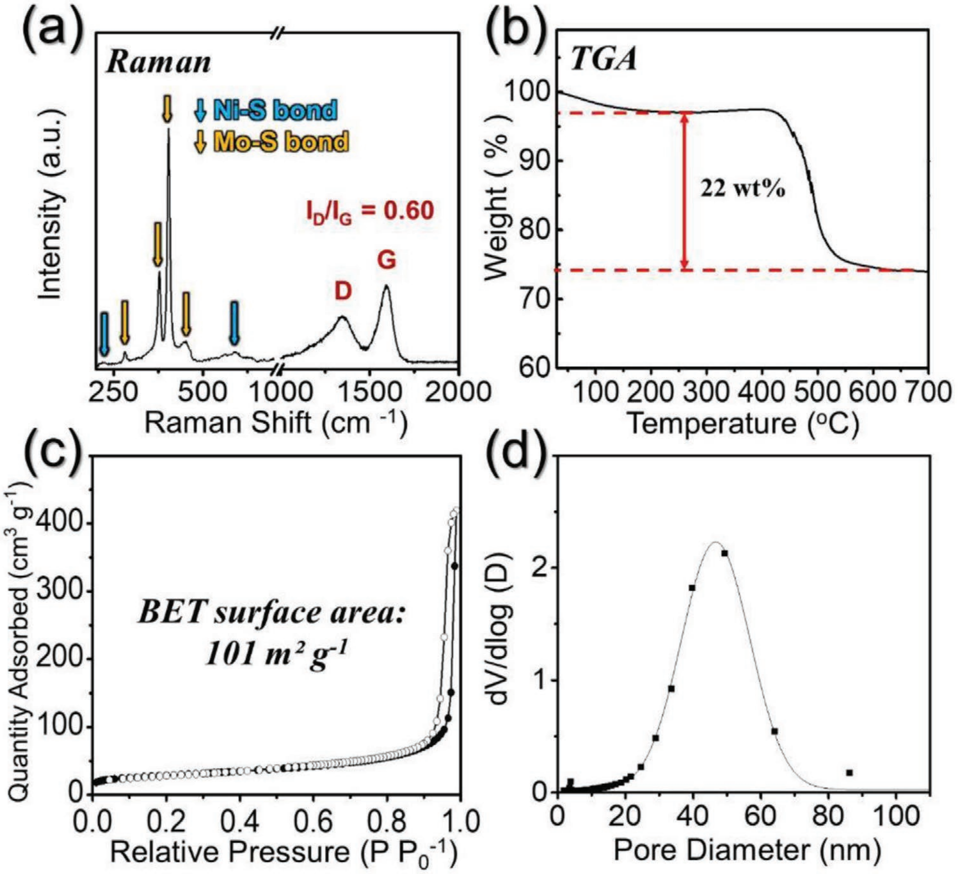

Figure 4. Characterization of P-NiMoS/C microspheres: a) Raman spectrum, b) TG curve, c) N_2 adsorption–desorption isotherms, and d) BJH desorption pore-size distribution.

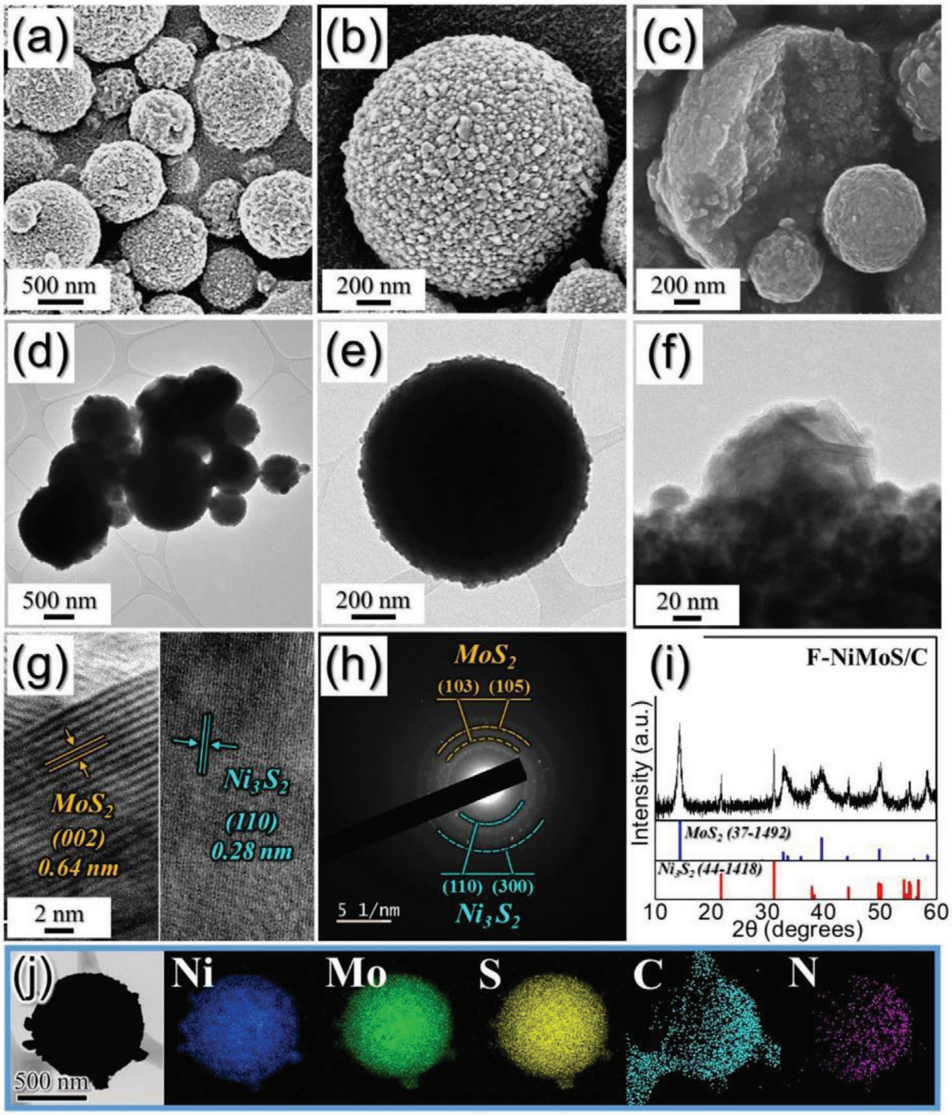

Figure 5. Morphologies, SAED, XRD patterns, and elemental mapping images of F-NiMoS/C microspheres prepared by spray pyrolysis and subsequent sulfidation at 500 °C: a,b) FE-SEM images, c) fractured sphere's FE-SEM image, d–f) TEM images, g) HR-TEM images, h) SAED pattern, i) XRD pattern, and j) elemental mapping images.

P-NiMoS/C microspheres (Figure 4c) suggest a high volume of gas adsorption due to the presence of ordered mesopores all over the internal and external surfaces, which resulted in a high Brunauer–Emmett–Teller (BET) surface area of 101 $m^2\ g^{-1}$. The Barrett–Joyner–Halenda pore size curve shown in Figure 4d clearly suggests a Lorentzian-type distribution with a peak maximum at 49 nm. This proves the well-developed ordered mesopores (pores with diameters between 2 and 50 nm) in the prepared composite microspheres. The uniformly distributed mesopores envisage better electrolyte percolation, leading to enhanced Na-ion diffusion.

For comparison, the powders obtained after spray pyrolysis using a spray solution containing Ni/Mo salts and PVP without PS nanobeads are shown in Figure S3, Supporting Information. The powders have a filled spherical morphology with no obvious presence of ordered mesopores throughout the structure (Figure S3a,b, Supporting Information). Additionally, the powders show a debossed surface structure, which is formed due to the PVP migration toward the shell part during the spray pyrolysis followed by thermal decomposition to carbon and subsequent structural shrinkage.[41] The XRD pattern presented in Figure S3c, Supporting Information, confirms the oxide phases of MoO_2, $NiMoO_4$, and metallic Ni. The obtained non-porous or filled composite precursor powders were further subjected to sulfidation at 500 °C to prepare F-NiMoS/C microspheres, as shown in **Figure 5**. The FE-SEM results (Figure 5a–c) suggest that F-NiMoS/C microspheres maintain the primary spherical morphology even after the sulfidation process with an average microsphere size of 0.9 µm (Figure S4a, Supporting Information). However, it can be seen that the nanocrystals with a size of ≈40 nm precipitated on the powder surface after sulfidation (Figure 5b). The TEM images shown in Figure 5d–f confirms the formation of non-aggregated and highly filled microspheres with no pore formation. The high-resolution TEM image (Figure 5g) indicates clear lattice fringes separated by 0.64 and 0.28 nm corresponding to the (002) and (110) lattice planes of the MoS_2 and Ni_3S_2 phases, respectively. In addition, the SAED pattern shown in Figure 5h confirms the high-resolution TEM results with well-distinguished diffraction rings that belong to nanocrystalline MoS_2 and Ni_3S_2. The XRD pattern (Figure 5i) also confirms the coexistence of bimetallic (Ni, Mo)-sulfide-based dual crystalline phases. However, it should be noted that the crystalline Ni—S phase (i.e., Ni_3S_2) in the F-NiMoS/C microspheres is different from that obtained in the P-NiMoS/C microspheres (i.e., Ni_7S_6), which is attributed to the difference in porosity level between the structures. As P-NiMoS/C is highly porous, the H_2S gas infiltrates well inside the structure, leading to more sulfidation compared to that of F-NiMoS/C. The poor sulfidation of F-NiMoS/C results in a sulfur-deficient phase. The elemental mapping results presented in Figure 5j indicate the homogeneous distribution of Ni_3S_2 and MoS_2 crystals in the carbon matrix. Furthermore, through an elemental analysis, the C and N contents in the F-NiMoS/C microspheres were determined to be 8 and 1 wt%, respectively (Table S1, Supporting Information), which suggests the presence of NGC in the F-NiMoS/C microspheres. However, a small amount of N-doping compared to P-NiMoS/C is also observed because N could not completely substitute C inside the filled structure during the heat treatment. Furthermore, the I_D/I_G ratio of the F-NiMoS/C microspheres (Figure S5, Supporting Information) was 0.61, indicating the graphitic nature of the carbon matrix in the F-NiMoS/C microspheres.

To further prove the structural superiority of P-NiMoS/C microspheres, non-porous and carbon-free F-NiMoS microspheres were also prepared. The precursor powders obtained after spray pyrolysis in an air atmosphere using a spray solution containing only Ni/Mo salts without PVP and PS nanobeads are shown in Figure S6, Supporting Information. The as-sprayed powders display microsphere morphology with highly aggregated precursor material all over the powder surface (Figure S6b, Supporting Information). The XRD pattern shown in Figure S6c, Supporting Information, indicates the formation of a bimetallic oxide with mixed phases of $NiMoO_4$. The obtained filled $NiMoO_4$ precursor powders were further subjected to sulfidation at 500 °C to prepare F-NiMoS microspheres, as shown in **Figure 6**. The low-resolution FE-SEM micrographs (Figure 6a) reveal that the sample possesses a microsphere morphology with a non-uniform size distribution (average diameter of about 0.8 µm as shown in Figure S4b, Supporting Information). In addition, the outer surface of the microspheres is covered with sheet-type crystals (Figure 6b), which is believed to be layered MoS_2-flakes, primarily obtained after the sulfidation process. The absence of carbon allowed the unrestricted crystal growth of MoS_2, which results in the flake-type formation. Furthermore, the fractured surface image in Figure 6c shows that the inner core of the microspheres is highly dense. The low-resolution TEM image (Figure 6d) also shows highly dense and slightly aggregated microspheres, which is consistent with the FE-SEM results. In addition, the formation of flake-type crystals on the outer surface of the microspheres is also evident (Figure 6e,f). The high-resolution TEM image (Figure 6g) clearly reveals the formation of layered-type lattice fringes separated by 0.64 nm, which is attributed to the (002) lattice plane of the MoS_2 flakes. The lattice fringe separated by 0.28 nm is assigned to the (110) lattice plane of the Ni_3S_2 phase. The SAED (Figure 6h) and XRD (Figure 6i) patterns further prove the formation of layered MoS_2 and Ni_3S_2 phases. The elemental mapping (Figure 6j) indicates the uniform distribution of the MoS_2 and Ni_3S_2 phases in the structure and additionally grown MoS_2-flakes covered on the sphere surface without carbon. The BET surface areas of the F-NiMoS and F-NiMoS/C microspheres were 14 and 35 $m^2\ g^{-1}$, respectively (Figure S7, Supporting Information), which are much smaller than that of P-NiMoS/C microspheres (101 $m^2\ g^{-1}$) owing to the absence of ordered mesopores.

Electrochemical performances of the P-NiMoS/C, F-NiMoS/C, and F-NiMoS microspheres were shown in **Figure 7**. Figure 7a shows the cyclic voltammetry (CV) results of the P-NiMoS/C microspheres for the first five cycles at a scan rate of 0.1 $mV\ s^{-1}$ in the voltage window of 0.001–3.0 V. During the first cathodic scan, the broad peak at 0.75 V indicates the reduction of MoS_2 and Ni_7S_6 components to form Mo and Ni nanocrystals, respectively, according to the following reaction: $MoS_2 + 4Na^+ + 4e^- \leftrightarrow Mo + 2Na_2S$ and $Ni_7S_6 + 12Na^+ + 12e^- \leftrightarrow 7Ni + 6Na_2S$.[10,27,30] In addition, the sharp cathodic peak at ≈0.002 V is due to the intercalation of Na^+ ions into the NGC matrix.[27] During the first anodic scan, the small voltage peak at 1.37 V is assigned to the oxidation of metallic Ni to Ni^+.[27] Upon further oxidation, Ni^+ is oxidized to Ni^{2+}, whereas the reduced Mo is converted to MoS_2 at 1.70 V.[27,42] From the second cycle onward, the cathodic peak shifted to a slightly higher voltage of 0.88 V owing to the formation of ultrafine nanocrystals of MoS_2 and Ni_7S_6, whereas the anodic peak appears at the same voltage with a slightly reduced current intensity.[27] Additionally, the exactly overlapped CV curves after the first cycle suggest reversible redox processes. Likewise, F-NiMoS/C and F-NiMoS microspheres also display similar CV characteristics, as shown in Figure S8, Supporting Information, owing to the similar crystal phases. However, the sharp cathodic peak at ≈0.002 V could be assigned to the sodium ion storage in the MoS_2 crystal structure and is in well accordance with the previous reports on MoS_2.[42,43] Figure 7b shows the initial charge–discharge profiles of the P-NiMoS/C, F-NiMoS/C, and F-NiMoS microspheres at a current density of 0.5 $A\ g^{-1}$. The obtained voltage profiles are consistent with the CV results with charge and discharge voltage plateaus at 1.7 and 0.8 V, respectively. In addition, the P-NiMoS/C microspheres display the lowest polarization potential (ΔV = 0.94 V) compared to those of F-NiMoS/C (ΔV = 1.10 V) and F-NiMoS (ΔV = 1.01 V) microspheres, as shown in Figure S9, Supporting Information. This clearly suggests that the superior electrolyte percolation due to ordered mesoporous and improved electronic/ionic conductivities due to NGC resulted in enhanced redox kinetics in the P-NiMoS/C microspheres compared to those in the F-NiMoS/C and F-NiMoS microspheres. As a result, the P-NiMoS/C microspheres exhibited the highest initial discharge capacity of 718 $mA\ h\ g^{-1}$ whereas the F-NiMoS/C and F-NiMoS microspheres exhibited initial discharge capacity of 494 and 468 $mA\ h\ g^{-1}$, respectively. Besides the Coulombic efficiencies for P-NiMoS/C, F-NiMoS/C, and F-NiMoS microspheres were

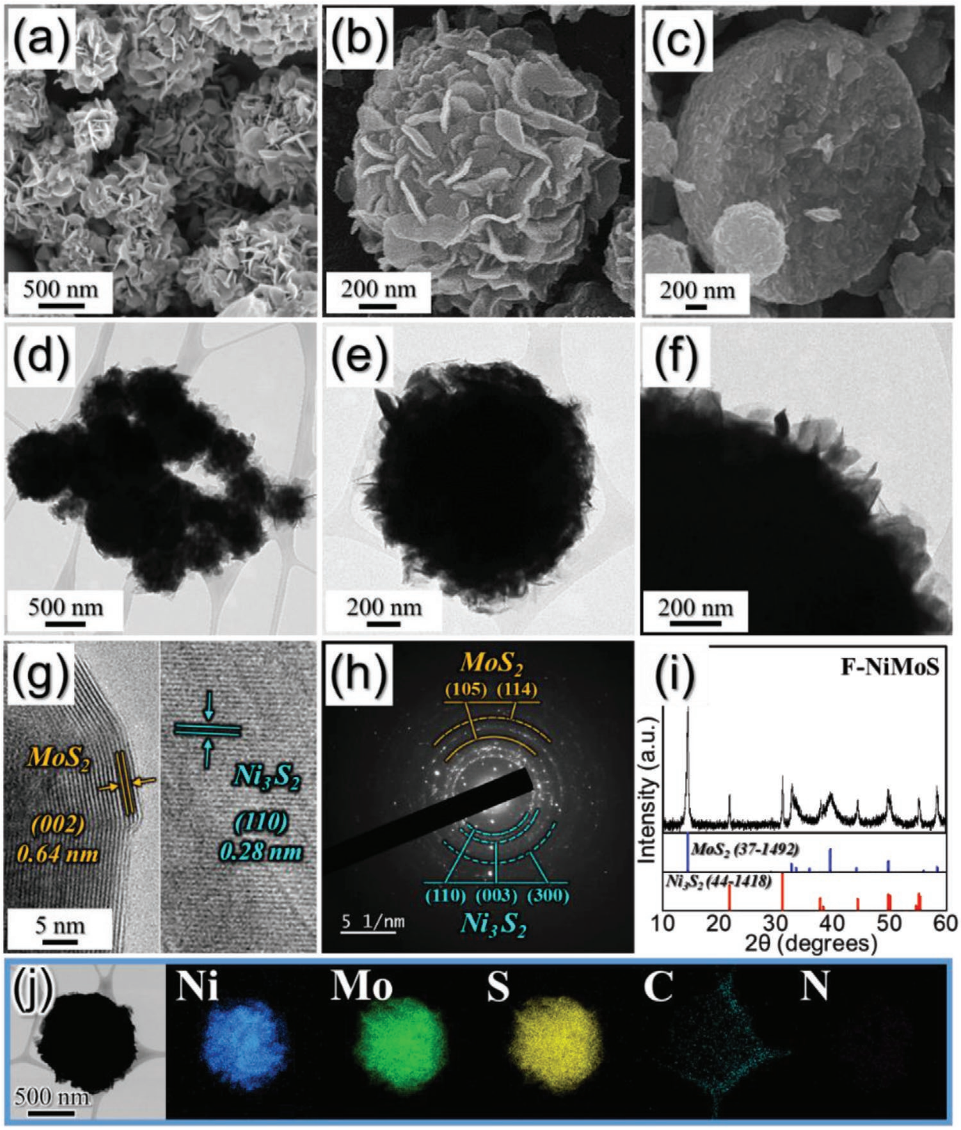

Figure 6. Morphologies, SAED, XRD patterns, and elemental mapping images of F-NiMoS microspheres prepared by spray pyrolysis and subsequent sulfidation at 500 °C, a,b) FE-SEM images, c) fractured sphere's FE-SEM image, d–f) TEM images, g) HR-TEM images, h) SAED pattern, i) XRD pattern, and j) elemental mapping images.

≈61%, 75%, and 74%, respectively. The slightly lower Coulombic efficiency for P-NiMoS/C is due to higher carbon content in the structure compared to others (Table S1, Supporting Information).

The cycling performances of the P-NiMoS/C, F-NiMoS/C, and F-NiMoS microspheres at a current density of 0.5 A g^{-1} were shown in Figure 7c. The P-NiMoS/C and F-NiMoS/C microspheres showed superior cycling performances than the F-NiMoS microspheres over 150 cycles because the carbon matrix could absorb the mechanical stress of the active materials induced by repeated Na^+ ion diffusion. Additionally, the growth of active materials surrounded by the carbon matrix was effectively inhibited, providing better tolerating volume changes associated with the phase transitions that occur during cycling. After 150 continuous charge/discharge cycles, the P-NiMoS/C, F-NiMoS/C, and F-NiMoS microspheres showed discharge capacities of 444, 272, and 280 mA h g^{-1}, respectively, and their capacity retention values measured from the second cycle were 98%, 73%, and 80%, respectively. On the other hand, the discharge capacity of the F-NiMoS microspheres initially increased up to approximately the 80th cycle and steadily decreased in subsequent cycles. The initial increase in capacity is due to the pulverization of the F-NiMoS microspheres with a large crystallite size, which leads to the generation of a fresh metal surface in every cathodic process as well as continuous reversible solid electrolyte interface layer formation.[26] Eventually, the repeated cycles caused structural destruction, resulting in capacity fading. Besides, the capacity contribution of each component in P-NiMoS/C, that is, MoS_2 and Ni_7S_6 was also calculated at a current density of 0.5 A g^{-1}. For the same, the weight percentage of MoS_2 and Ni_7S_6 samples were first calculated using inductively coupled plasma-optical emission spectrometry (ICP-OES)

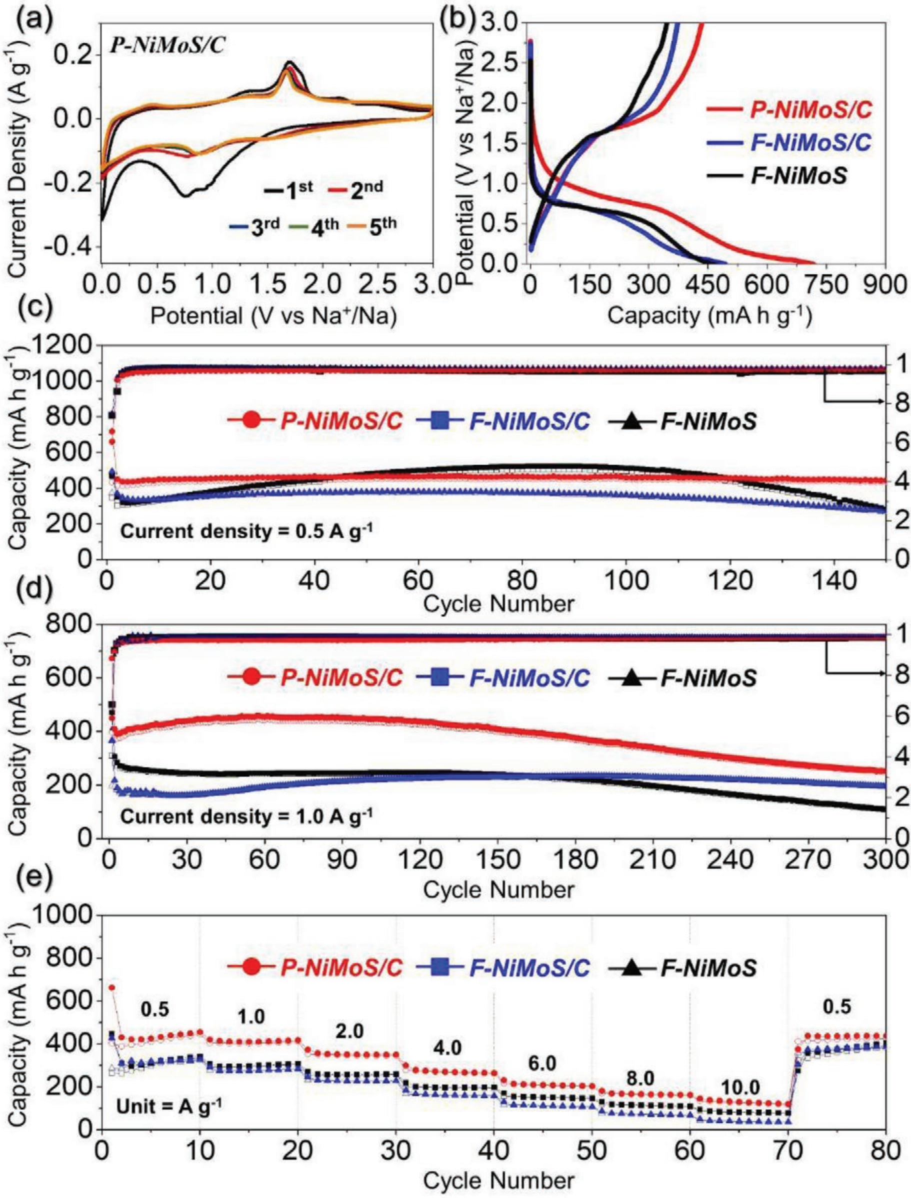

Figure 7. Electrochemical properties of P-NiMoS/C, F-NiMoS/C, and F-NiMoS microspheres: a) CV curves of P-NiMoS/C, b) initial discharge/charge curves at a constant current density of 0.5 A g^{-1}, c) cycle performances at a current density of 0.5 A g^{-1}, d) cycle performances at a current density of 1.0 A g^{-1}, and e) rate performances.

technique (Table S2, Supporting Information). From ICP-OES results, the composition of the P-NiMoS/C sample was found to be primarily composed of MoS_2 and Ni_7S_6 only with a weight percentage of ≈44.83% and 36.13%, respectively. The MoS_2 and Ni_7S_6 samples were prepared separately using identical spray-pyrolysis technique with same heat treatment conditions and were subjected to physical and electrochemical characterizations as shown in Figures S10 and S11, Supporting Information, respectively. The observed discharge capacity for P-NiMoS/C sample at 0.5 A g^{-1} at 50th cycle was ≈464.4 mA h g^{-1} which originated due to the collective capacity contribution of MoS_2, and Ni_7S_6 in 41.96% and 37.53%, respectively, at identical current density and cycle number. Figure 7d shows the cycling performances of the microspheres at a higher current density of 1.0 A g^{-1}. P-NiMoS/C microspheres showed the highest initial discharge capacity of 673 mA h g^{-1} whereas the F-NiMoS/C and F-NiMoS microspheres showed initial discharge capacity of 367 and 471 mA h g^{-1}, respectively. In addition, the initial capacity increase for P-NiMoS/C and F-NiMoS/C microspheres for several tens of cycles is mainly due to the formation of a polymeric gel-like film on the microspheres surface as reported previously.[44–46] Furthermore, F-NiMoS microspheres show slightly stable cycling performance compared to the P-NiMoS/C microspheres till 150th cycle that might be due to the substantial redox reactions taking place at the surface of the dense microspheres compared to the bulk. Although, these surface reactions start fading after 150 cycles mainly due to the structure collapse of the microspheres that arises from the volume stress over repeated cycling. The P-NiMoS/C, F-NiMoS/C, and F-NiMoS microspheres delivered discharge capacities of 252, 196, and 110 mA h g^{-1}, respectively at the end of the 300th cycle, and the capacity retention values measured from the second cycle were 62%, 90%, and 36%, respectively. Despite the high current density of 1.0 A g^{-1}, the higher specific capacity of P-NiMoS/C microspheres compared to F-NiMoS/C and F-NiMoS could be attributed to the following factors: 1) a highly ordered mesoporous nanostructure that not only allows smooth Na$^+$ ion diffusion owing to better electrode wetting or electrolyte percolation but also accommodates the large volume strain during the prolonged cycling; 2) the higher electrical conductivity of NGC, leading to fast charge transfer during the redox processes. In addition, to calculate the capacity contribution of the NGC matrix in the total capacity, the P-NiMoS/C microspheres were treated with highly concentrated (6.0 M) hydrochloric acid for 3 days to remove the respective Ni, Mo, and S species followed by repeated washing using distilled water and subsequent drying at 100 °C overnight. The obtained physical and electrochemical results are summarized in Figure S12, Supporting Information. The FE-SEM micrographs (Figure S12a, Supporting Information) suggest that the sample morphology remains intact even after the etching process and mainly includes NGC as indicated by the EDS spectrum (Figure S12b, Supporting Information). The CV curves obtained at 0.1 mV s^{-1} (Figure S12c, Supporting Information) clearly confirm the above results as only single cathodic peak was observed at 0.002 V which corresponds to the sodium intercalation in the carbon matrix.[27] These results are further supported by the initial charge/discharge (Figure S12d, Supporting Information) and the cycling performance (Figure S12e, Supporting Information) obtained at 0.5 A g^{-1}. The cycling performance suggests that the NGC matrix displays a low discharge capacity of ≈83 mA h g^{-1} at 50th cycle which is around 18% of the P-NiMoS/C microspheres at the identical current density and cycle number (Figure 7c). Therefore, these results suggest that the NGC matrix only acts as a conductive scaffold for rapid charge transfer during the electrochemical process.

Figure 7e shows the rate performances of the microspheres at current densities ranging from 0.5 to 10.0 A g^{-1}. The initial discharge capacities of the P-NiMoS/C microspheres at current densities of 0.5, 1.0, 2.0, 4.0, 6.0, 8.0, and 10.0 A g^{-1} were determined to be 662, 419, 373, 300, 231, 181, and 146 mA h g^{-1}, respectively. These are much higher than F-NiMoS/C and F-NiMoS which exhibit discharge capacities of 426/446, 292/307, 245/271, 184/218, 130/170, 86/130, and 49/94 mA h g^{-1}, respectively, at identical current densities. The high-rate performance also proves the structural superiority of the P-NiMoS/C microspheres over the F-NiMoS/C and F-NiMoS microspheres. The efficient penetration of the liquid electrolyte into the electrode during cycling was possible owing to its 3-DOM architecture, which promoted the electrochemical reaction. Additionally, the NGC matrix contributed to the high electrical conductivity of the electrode, which facilitated rapid electron transfer by improving the electrical contact between the active sites of the MoS$_2$ and Ni$_7$S$_6$ nanocrystals constituting the P-NiMoS/C microspheres and the electrode. At a reverse current density of 0.5 A g^{-1}, a stable discharge capacity of 435 mA h g^{-1} was recovered for the P-NiMoS/C microspheres. The electrochemical performance of the P-NiMoS/C microspheres was compared with those of other reported Ni-, Mo-, and bimetallic (Ni, Mo) sulfide nanostructures with various morphologies, as summarized in Table S3, Supporting Information. P-NiMoS/C microspheres prepared in this study showed superior electrochemical properties for Na ion storage even at high current density.

To better understand the electrochemical kinetics inside the cell, CV curves were plotted for P-NiMoS/C microspheres in the voltage window of 0.001–3.0 V at different scan rates, as shown in **Figure 8**a. In addition, to differentiate between the diffusion and capacitive-controlled reactions, the peak current (i) value during the redox reactions was plotted against the scan rates (ν) according to the following power-law equation:[26,47]

$$i = a\nu^b \tag{1}$$

$$\log(i) = b\log(\nu) + \log(a) \tag{2}$$

Here, the variables a and b determine whether the process is diffusion-controlled or capacitive-controlled. The redox process is mainly capacitive if b approaches 1.0, whereas it is mainly diffusion-controlled if b approaches 0.5.[47] The slope of the log(i) versus log(ν) plot determines the b values, as shown in Figure 8b. The b-values for the four different redox peaks in the P-NiMoS/C microspheres are close to 1, indicating a capacitive-dominant process. In contrast, the reaction dynamics for the F-NiMoS/C microspheres shown in Figure S13a,b, Supporting Information, display lower b values, suggesting a marginally lower capacitive-controlled redox process. Likewise, the F-NiMoS microspheres shown in Figure S13c,d, Supporting Information, exhibited the lowest b values among the samples, indicating that the redox processes are still governed by a capacitive process but to a lower extent. To quantify the capacitive contribution in the P-NiMoS/C microspheres, the capacitive and diffusion-controlled processes were separated from the total charge stored using the following equation:[26,48,49]

$$i = k_1\nu + k_2\nu^{1/2} \tag{3}$$

where $k_1\nu$ and $k_2\nu^{1/2}$ represent the capacitive and diffusion contributions, respectively, and k_1 and k_2 are constants that can be obtained from the slope and intercept of the $i(V)/\nu^{1/2}$ versus $\nu^{1/2}$ plot, respectively. As shown in Figure 8c, the capacitive contribution factor ($k_1\nu$) highlighted by the red region is 88% at a scan rate of 2.0 mV s^{-1}. Figure 8d shows the capacitive fraction of the P-NiMoS/C microspheres at scan rates other than 2.0 mV s^{-1}. Furthermore, the surface-controlled reaction contributions in the F-NiMoS/C and F-NiMoS microspheres shown in Figures 8e,f and 8g,h, respectively, suggest a lower percentage of the capacitive process compared to the P-NiMoS/C microspheres. These results imply kinetically favored rapid Na$^+$ ion transport for P-NiMoS/C microspheres owing to the better electrolyte percolation, efficient mitigation of volume variation during cycling, and highly conducting NGC-network that facilitates rapid charge transfer.

Figure 9 shows the results of electrochemical impedance spectroscopy (EIS) tests of the assembled cells in the fully

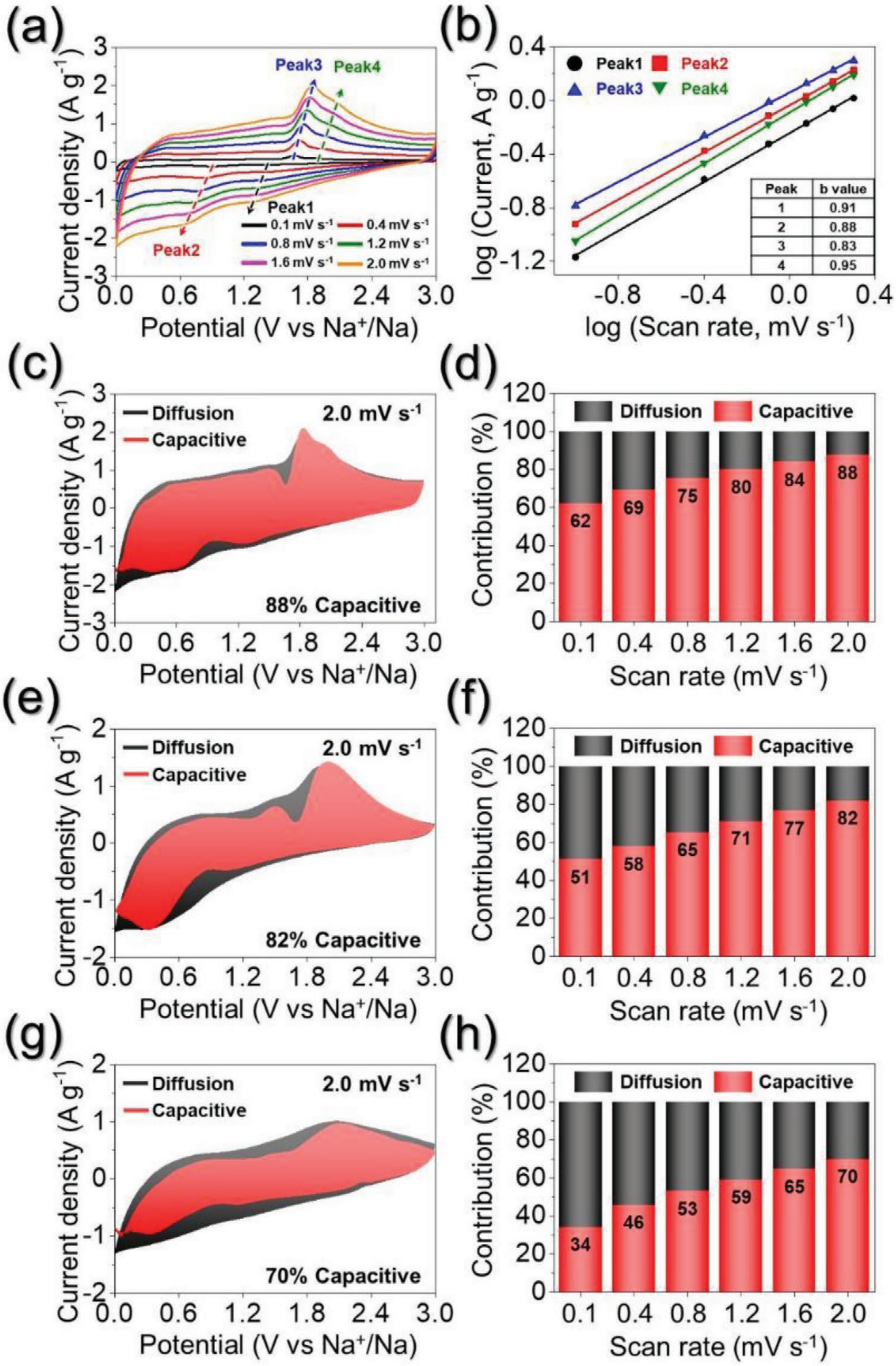

Figure 8. Electrochemical reaction dynamics analysis of a–d) P-NiMoS/C, e,f) F-NiMoS/C, and g,h) F-NiMoS microspheres: a) CV curves obtained at various scan rates, b) current response (*i*) versus scan rate (*n*) at each redox peak, c,e,g) CV curves with the capacitive fraction shown by the red region at a scan rate of 2.0 mV s^{-1}, and d,f,h) bar charts showing the percentage of the capacitive contribution at different scan rates.

charged state, which were performed to further validate the structural advantages and excellent Na ion storage capability of the P-NiMoS/C microspheres. The Nyquist plots for fresh cells (Figure 9a) suggest marginally different solution resistance (R_s) values that lie in the range of 17–25 Ω, indicating slightly different electrode–electrolyte interface reactions. Furthermore, the charge transfer resistance (R_{ct}) values for P-NiMoS/C, F-NiMoS/C, and F-NiMoS microspheres were 159, 426, and

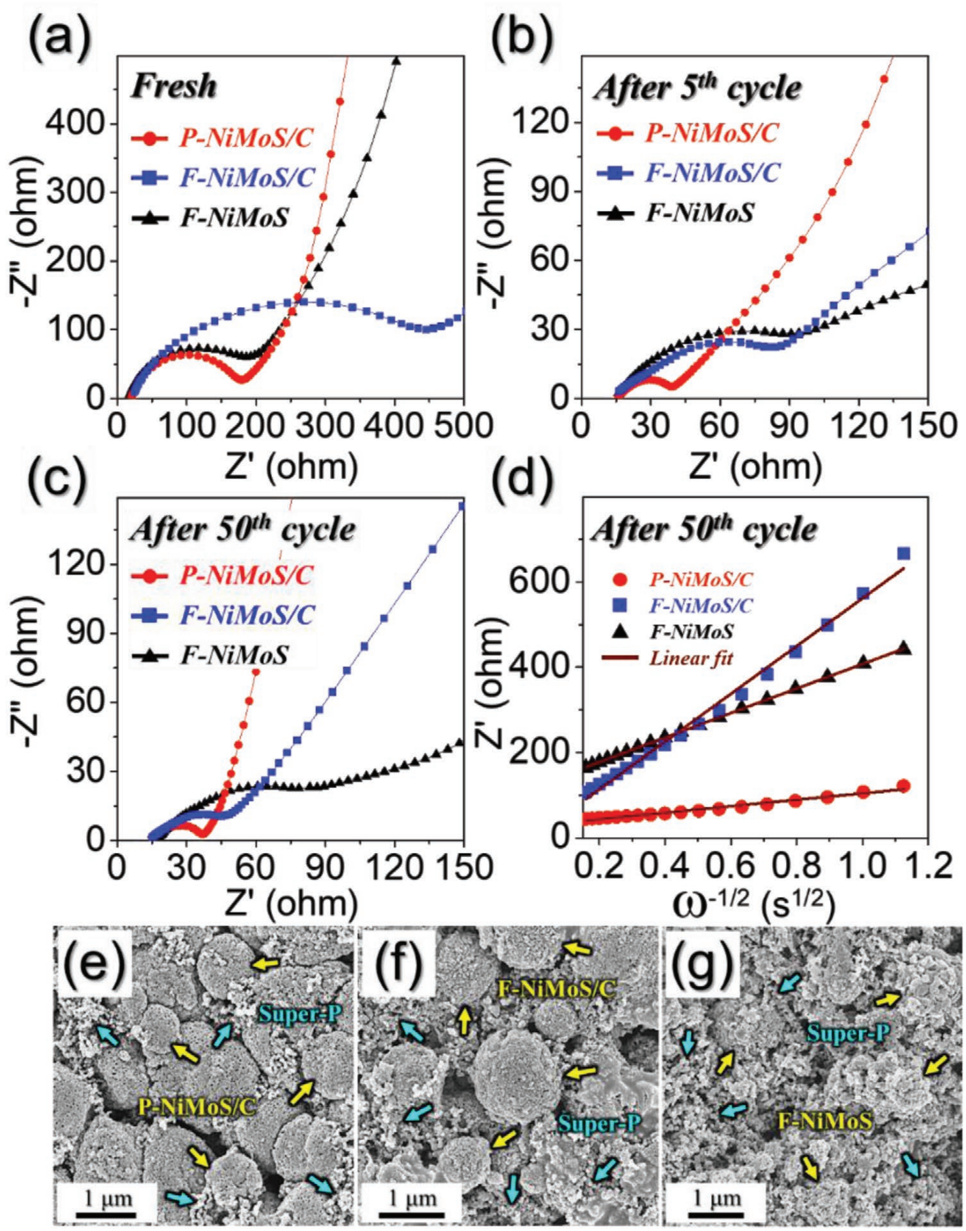

Figure 9. a–d) Nyquist impedance plots and e–g) FE-SEM images of P-NiMoS/C, F-NiMoS/C, and F-NiMoS microspheres obtained after 100th cycles at 1.0 A g^{-1}: a) before cycling, b) after 5th cycle, c) after 50th cycle, d) relationships between the real part of the impedance (Z_{re}) and $\omega^{-1/2}$ of the samples obtained after 50th cycles. e) P-NiMoS/C, f) F-NiMoS/C, and g) F-NiMoS microspheres.

169 Ω, respectively. However, after the fifth cycle, all samples displayed a substantial decrease in R_{ct} values. After the 50th cycle, the R_{ct} values decreased to 22, 30, and 68 Ω for the P-NiMoS/C, F-NiMoS/C, and F-NiMoS microspheres, respectively. The lower R_{ct} value for the P-NiMoS/C microspheres over cycling suggests their faster redox kinetics and superior electrode integrity. Figure 9d shows plots of Z_{re} as a function of $\omega^{-1/2}$ ($\omega = 2\pi f$ is the angular frequency) in the low-frequency region after the 50th cycle. The less steep slope at low frequencies for the P-NiMoS/C microspheres indicates higher Na ion diffusivity in the structure compared to the F-NiMoS/C and F-NiMoS microspheres.

Furthermore, the Na ion diffusion coefficient (D_{Na+}) values were further calculated from Figure 9d using the following equation:[50–52]

$$D_{Na+} = 0.5R^2T^2/A^2F^4C^2\sigma_W^2 \tag{4}$$

where D_{Na+} is the sodium-ion diffusion coefficient, R is the gas constant, T is the temperature, A is the electrode area, C is the Na$^+$ ion concentration, F is the Faraday constant, and σ_W is the Warburg impedance factor. The D_{Na+} values for the P-NiMoS/C, F-NiMoS/C, and F-NiMoS microspheres were 1.85 × 10^{-10}, 2.50 × 10^{-11}, and 4.87 × 10^{-11} cm^2 s^{-1}, respectively. Thus, the D_{Na+}

value of the P-NiMoS/C microspheres was one order of magnitude higher than that of the other microsphere, indicating much faster Na ion diffusion and, therefore, superior redox reaction kinetics during the charge–discharge process. To confirm the structural stability, morphology of each microsphere after cycling was obtained at the end of 100th cycle at a current density of 1.0 A g^{-1}, as shown in Figure 9e–g. The FE-SEM images of the P-NiMoS/C and F-NiMoS/C microspheres (Figure 9e,f) after cycling indicate that the microspheres maintain a spherical morphology throughout the external surface, implying high structural integrity of the prepared microspheres, which might be due to the inability of the structure to accommodate the volume stress induced by Na ion diffusion during prolonged cycling. However, F-NiMoS microspheres (Figure 9g) reveal the complete degradation of the structure into a highly aggregated powder-type morphology owing to the inability to withstand the volume variation. Overall, we believe that the synthesis of 3-DOM nanostructures with a highly stable biphasic structure and NGC layer as a conductive scaffold resulted in high structural stability that not only tolerated the severe volume variation during repeated cycling but also provided conductive pathways for faster Na ion transfer, leading to superior electrochemical performance.

3. Conclusions

In summary, we employed a mesoporous and bimetallic (Ni, Mo)-sulfide-based nanostructure with NGC as an advanced anode material for NIBs. The P-NiMoS/C microspheres were prepared by an easily scalable spray pyrolysis technique followed by a one-step heat-treatment process for sulfidation. The obtained microspheres possess highly ordered mesopores throughout the internal and external structures due to the decomposition of PS nanobeads. Moreover, the combustion of PVP in N_2 atmosphere results in the formation of a highly conductive NGC skeleton. The stable phases of nanocrystalline MoS_2 and Ni_7S_6 formed during sulfidation were surrounded by a carbon matrix, which efficiently prevented their crystal growth in the composite. The presence of ordered mesopores, nanocrystalline bimetallic (Ni, Mo)-sulfides, and conductive NGC play a key role in the overall improvement of the cell performance; the ordered mesopores provide sufficient space to sustain volume variations during prolonged cycling, whereas the conductive carbon provides numerous conductive channels for rapid charge transfer. As a result, the rationally designed nanostructure resulted in superior electrochemical performance with high rate capability and stable prolonged cycling performance owing to the higher ability to alleviate volume variations compared to the F-NiMoS/C and F-NiMoS microspheres. The results of this study will provide considerable insights for the development of advanced anodes based on the multicomponent strategy for various rechargeable energy storage systems.

4. Experimental Section

Sample Preparation: The P-NiMoS/C, F-NiMoS/C, and F-NiMoS microspheres were prepared by a spray pyrolysis process followed by a sulfidation process. Briefly, 10.0 g of $Ni(NO_3)\cdot 6H_2O$ (DAEJUNG, >97.0%, Mw = 290.79) and 6.0 g of $(NH_4)_6Mo_7O_{24}\cdot 4H_2O$ (DAEJUNG, >98.0%, Mw = 1235.86) were dissolved in 200 mL of distilled water and stirred for 1 h followed by the addition of 4.0 g of PVP (DAEJUNG, Mw = 40000). The obtained solution was stirred vigorously for 2 h followed by the addition of PS nanobeads suspension (200 mL, $\phi = 100$ nm). The PS nanobeads were used as a pore generator and prepared using an emulsion polymerization technique reported in the authors' previous work.[53] The obtained final spray solution was stirred overnight at room temperature. Afterward, the solution was transferred to an ultrasonic nebulizer connected to a vertical quartz reactor (Scheme S1, Supporting Information). The droplets generated by the nebulizer were fed through a quartz reactor fixed at 700 °C in a N_2 atmosphere (10 L min^{-1}). The as-prepared powders obtained after spray pyrolysis were subjected to an additional heat treatment in the tubular furnace for the sulfidation process. Thiourea was used as the sulfur source in the form of H_2S gas, and the temperature was increased to 500 °C at a heating rate of 5 °C min^{-1} h and stayed for 6 h in a slightly reductive atmosphere (5% H_2/Ar mixture gas). The final product was denoted as P-NiMoS/C microspheres. Additionally, another sample without PS nanobeads was also prepared under identical synthesis conditions and named as F-NiMoS/C. Moreover, a standard sample without mesopores and carbon using the spray solution without PS nanobeads and PVP was also prepared under identical temperature conditions in air atmosphere and denoted as F-NiMoS.

Characterization: The morphological features of the prepared microspheres were analyzed using FE-SEM (Zeiss, Ultra Plus) and field-emission transmission electron microscopy (JEOL, JEM-2100F). The phase and crystal structure of the microspheres were determined using XRD analyses (Bruker, D8 Discover). The chemical environment of all the elements in the as-synthesized microspheres was determined using XPS using a monochromatic Al-Kα X-ray source. A BET analysis was performed to determine the surface area and pore volume of the microspheres using a porosity analyzer. TG analyses were carried out in an air atmosphere with temperature increasing from room temperature to 700 °C at a ramp rate of 10 °C min^{-1} to quantify the carbon content. ICP-OES technique was used to analyze the elemental composition of the prepared samples. A Raman spectroscopy (LabRam, HR800, Horiba Jobin-Yvon) analysis was performed to investigate the crystallinity of the carbonaceous materials in the prepared microspheres.

Electrochemical Measurements: To analyze the electrochemical performance of the as-prepared samples, 2032-type coin cells were assembled inside a glove box. The electrodes were prepared using a slurry casting method by mixing the as-prepared microspheres as the active material, carbon black (super-P) as a conductive agent, and sodium carboxymethyl cellulose as a binder in a 7:2:1 ratio in an appropriate amount of deionized water. The obtained slurry was cast on a copper current collector using a doctor blade and dried at 60 °C overnight in a hot air oven. Circular electrodes ($\phi = 14$ mm) were punched and transferred to a glove box. Coin cells (CR2032) were assembled using Na metal and a microporous polypropylene film as the counter electrode and separator, respectively. The electrolyte used was 1.0 M $NaClO_4$ in a mixture of ethylene carbonate and dimethyl carbonate (1:1 by volume) with 5 wt% fluoroethylene carbonate as an additive. The assembled cells were analyzed using CV at a scan rate of 0.1 mV s^{-1}. The cells were cycled at various current densities from 0.5 to 10.0 A g^{-1}. The voltage window throughout the electrochemical tests was fixed at 0.001–3.0 V. EIS data was collected in the frequency range of 100 kHz–0.01 Hz.

Supporting Information

Supporting Information is available from the Wiley Online Library or from the author.

Acknowledgements

J.S.L. and R.S. contributed equally to this work. This work was supported by the National Research Foundation of Korea (NRF) grant funded by the Korean government (MSIP) (Nos. NRF-2017M1A2A2087577, NRF-2021R1A4A200168711, and NRF-2021R1I1A3057700) and Innopolis Foundation through Technology Commercialization Project, funded by Ministry of Science and ICT (202000145).

Conflict of Interest

The authors declare no conflict of interest.

Data Availability Statement

Research data are not shared.

Keywords

anode materials, bimetallic sulfides, Na-ion batteries, spray pyrolysis, three-dimensional ordered mesoporous microspheres

Received: February 18, 2021
Revised: June 18, 2021

[1] J. Wu, J. Liu, J. Cui, S. Yao, M. Ihsan-Ul-Haq, N. Mubarak, E. Quattrocchi, F. Ciucci, J.-K. Kim, *J. Mater. Chem. A* **2020**, *8*, 2114.
[2] Y. Sun, Y. Yang, X.-L. Shi, G. Suo, H. Chen, M. Noman, X. Tao, Z.-G. Chen, *Chem. Eng. J. Adv.* **2020**, *4*, 100053.
[3] D. T. Tran, H. Dong, S. D. Walck, S. S. Zhang, *RSC Adv.* **2015**, *5*, 87847.
[4] Y. Wang, J. Zhou, J. Wu, F. Chen, P. Li, N. Han, W. Huang, Y. Liu, H. Ye, F. Zhao, *J. Mater. Chem. A* **2017**, *5*, 25618.
[5] M.-C. Liu, H. Zhang, Y.-X. Hu, C. Lu, J. Li, Y.-G. Xu, L.-B. Kong, *Sustainable Energy Fuels* **2019**, *3*, 1239.
[6] B. Gendensuren, C. He, E.-S. Oh, *Korean J. Chem. Eng.* **2020**, *37*, 366.
[7] J. Chen, Z. Tang, Z. Pan, W. Shi, Y. Wang, Z. Q. Tian, P. K. Shen, *Mater. Des.* **2020**, *192*, 108780.
[8] X. Dong, Z. Xing, G. Zheng, X. Gao, H. Hong, Z. Ju, Q. Zhuang, *Electrochim. Acta* **2020**, *339*, 135932.
[9] S. H. Oh, J. K. Kim, Y. C. Kang, J. S. Cho, *Nanoscale* **2018**, *10*, 18734.
[10] X. Xie, Z. Ao, D. Su, J. Zhang, G. Wang, *Adv. Funct. Mater.* **2015**, *25*, 1393.
[11] Z. Yao, K. Zhu, X. Li, J. Wang, K. Yan, J. Liu, *J. Alloys Compd.* **2020**, *838*, 155541.
[12] Y. Su, C. Wu, H. Li, F. Chen, Y. Guo, L. Yang, S. Xu, *J. Alloys Compd.* **2020**, *845*, 156229.
[13] J. Ma, M. Xing, L. Yin, K. S. Hui, K. N. Hui, *Appl. Surf. Sci.* **2021**, *536*, 147735.
[14] M. S. Jo, J. S. Lee, S. Y. Jeong, J. K. Kim, Y. C. Kang, D. W. Kang, S. M. Jeong, J. S. Cho, *Small* **2020**, *16*, 2003391.
[15] J. Mohanta, H.-J. Kim, S. M. Jeong, J. S. Cho, H.-J. Ahn, J.-H. Ahn, J.-K. Kim, *Chem. Eng. J.* **2020**, *391*, 123510.
[16] S. Y. Jeong, S. Ghosh, J.-K. Kim, D.-W. Kang, S. M. Jeong, Y. C. Kang, J. S. Cho, *J. Ind. Eng. Chem.* **2019**, *75*, 100.
[17] S. H. Oh, J. S. Cho, *J. Alloys Compd.* **2019**, *806*, 1029.
[18] S. H. Oh, M. S. Jo, S. M. Jeong, Y. C. Kang, J. S. Cho, *Chem. Eng. J.* **2019**, *368*, 438.
[19] K. C. Wasalathilake, N. Hu, S. Fu, J.-c. Zheng, A. Du, C. Yan, *Appl. Surf. Sci.* **2021**, *536*, 147779.
[20] Y. Huang, D. Xiong, X. Li, H. M. K. Sari, J. Peng, Y. Li, Y. Li, D. Li, Q. Sun, X. Sun, *Front. Chem.* **2020**, *8*, 1.
[21] N. Dominguez, B. Torres, L. A. Barrera, J. E. Rincon, Y. Lin, R. R. Chianelli, M. A. Ahsan, J. C. Noveron, *ACS Omega* **2018**, *3*, 10243.
[22] E. Lim, J. Chun, C. Jo, J. Hwang, *Korean J. Chem. Eng.* **2021**, *38*, 227.
[23] A. Nulu, V. Nulu, K. Y. Sohn, *Korean J. Chem. Eng.* **2020**, *37*, 1795.
[24] J. Lv, D. Bai, L. Yang, Y. Guo, H. Yan, S. Xu, *Chem. Commun.* **2018**, *54*, 8909.
[25] Y. Lin, Z. Qiu, D. Li, S. Ullah, Y. Hai, H. Xin, W. Liao, B. Yang, H. Fan, J. Xu, *Energy Storage Mater.* **2018**, *11*, 67.
[26] J. S. Lee, M. S. Jo, R. Saroha, D. S. Jung, Y. H. Seon, J. S. Lee, Y. C. Kang, D. W. Kang, J. S. Cho, *Small* **2020**, *16*, 2002213.
[27] J.-S. Park, Y. C. Kang, *J. Mater. Chem. A* **2017**, *5*, 8616.
[28] K. Jayaramulu, J. Masa, O. Tomanec, D. Peeters, V. Ranc, A. Schneemann, R. Zboril, W. Schuhmann, R. A. Fischer, *Adv. Funct. Mater.* **2017**, *27*, 1700451.
[29] T.-W. Lin, C.-S. Dai, K.-C. Hung, *Sci. Rep.* **2014**, *4*, 1.
[30] G. D. Park, J. S. Cho, Y. C. Kang, *Nanoscale* **2014**, *7*, 16781.
[31] J. Lin, P. Wang, H. Wang, C. Li, X. Si, J. Qi, J. Cao, Z. Zhong, W. Fei, J. Feng, *Adv. Sci.* **2019**, *6*, 1900246.
[32] J. Lin, Y. Yan, X. Zheng, Z. Zhong, Y. Wang, J. Qi, J. Cao, W. Fei, Y. Huang, J. Feng, *J. Colloid Interface Sci.* **2019**, *536*, 456.
[33] Z. Tan, Y. Huang, S. Wang, C. Feng, Z. Sun, H. Wu, Y. Zhang, *Ionics* **2019**, *25*, 3961.
[34] W. Shuang, H. Huang, L. Kong, M. Zhong, A. Li, D. Wang, Y. Xu, X.-H. Bu, *Nano Energy* **2019**, *62*, 154.
[35] H. Dong, C. Liu, H. Ye, L. Hu, B. Fugetsu, W. Dai, Y. Cao, X. Qi, H. Lu, X. Zhang, *Sci. Rep.* **2015**, *5*, 1.
[36] B. Lu, J. Liu, R. Hu, H. Wang, J. Liu, M. Zhu, *Energy Storage Mater.* **2018**, *14*, 118.
[37] R. Saroha, A. K. Panwar, *J. Phys. D: Appl. Phys.* **2017**, *50*, 255501.
[38] Y. Yao, K. Ao, P. Lv, Q. Wei, *Nanomaterials* **2019**, *9*, 844.
[39] N. Feng, D. Hu, P. Wang, X. Sun, X. Li, D. He, *Phys. Chem. Chem. Phys.* **2013**, *15*, 9924.
[40] J. Wang, J. Liu, H. Yang, D. Chao, J. Yan, S. V. Savilov, J. Lin, Z. X. Shen, *Nano Energy* **2016**, *20*, 1.
[41] J. S. Cho, J. M. Won, J.-H. Lee, Y. C. Kang, *Nanoscale* **2015**, *7*, 19620.
[42] J. Wang, C. Luo, T. Gao, A. Langrock, A. C. Mignerey, C. Wang, *Small* **2015**, *11*, 473.
[43] Z. Wang, T. Chen, W. Chen, K. Chang, L. Ma, G. Huang, D. Chen, J. Y. Lee, *J. Mater. Chem. A* **2013**, *1*, 2202.
[44] Z.-S. Wu, W. Ren, L. Wen, L. Gao, J. Zhao, Z. Chen, G. Zhou, F. Li, H.-M. Cheng, *ACS Nano* **2010**, *4*, 3187.
[45] G. Zhou, D.-W. Wang, F. Li, L. Zhang, N. Li, Z.-S. Wu, L. Wen, G. Q. Lu, H.-M. Cheng, *Chem. Mater.* **2010**, *22*, 5306.
[46] J.-S. Do, C.-H. Weng, *J. Power Sources* **2005**, *146*, 482.
[47] J. Mei, T. He, Q. Zhang, T. Liao, A. Du, G. A. Ayoko, Z. Sun, *ACS Appl. Mater. Interfaces* **2020**, *12*, 21720.
[48] M. Wang, Y. Zhao, X. Zhang, R. Qi, S. Shi, Z. Li, Q. Wang, Y. Zhao, *Electrochim. Acta* **2018**, *272*, 184.
[49] H. Zhang, H. He, J. Luan, X. Huang, Y. Tang, H. Wang, *J. Mater. Chem. A* **2018**, *6*, 23318.
[50] R. Saroha, A. Gupta, A. K. Panwar, *J. Alloys Compd.* **2017**, *696*, 580.
[51] R. Saroha, A. K. Panwar, Y. Sharma, P. K. Tyagi, S. Ghosh, *Appl. Surf. Sci.* **2017**, *394*, 25.
[52] M. Yousaf, Y. Wang, Y. Chen, Z. Wang, A. Firdous, Z. Ali, N. Mahmood, R. Zou, S. Guo, R. P. Han, *Adv. Energy Mater.* **2019**, *9*, 1900567.
[53] M. S. Jo, S. Ghosh, S. M. Jeong, Y. C. Kang, J. S. Cho, *Nano-Micro Lett.* **2019**, *11*, 1.